Selectivity of the Br $3d^{-1}$ Auger decays in HBr

J. Palaudoux,[1] T. Kaneyasu,[2] L. Andric,[1,3] S. Carniato,[1] G. Gamblin,[1] F. Penent,[1] Y. Hikosaka,[4] E. Shigemasa,[5] K. Ito,[6] S. Fritzsche,[7,8] E. Kukk,[9] S. Sheinerman,[10] R. F. Fink,[11,*] P. Lablanquie,[1,*] and R. Püttner[12,*]

[1]*Sorbonne Université, Laboratoire de Chimie Physique-Matière et Rayonnement, Unité Mixte de Recherche du Centre National de la Recherche Scientifique (UMR 7614), 4 place Jussieu, 75005 Paris, France*
[2]*SAGA Light Source, Tosu 841-0005, Japan*
[3]*Université Paris-Est, 5 boulevard Descartes, F-77454 Marne-la Vallée Cedex 2, France*
[4]*Institute of Liberal Arts and Sciences, University of Toyama, Toyama 930-0194, Japan*
[5]*UVSOR Facility, Institute for Molecular Science, Okazaki 444-8585, Japan*
[6]*Synchrotron SOLEIL, l'Orme des Merisiers, Saint-Aubin, BP 48, 91192 Gif-sur-Yvette Cedex, France*
[7]*Helmholtz Institut Jena, 07743 Jena, Germany*
[8]*Theoretisch-Physikalisches Institut, Universität Jena, Fröbelstieg 3, 07743 Jena, Germany*
[9]*Department of Physics and Astronomy, University of Turku, FIN-20014 Turku, Finland*
[10]*Department of Physics, Saint Petersburg State Marine Technical University, 190121 Saint Petersburg, Russia*
[11]*Institut für Physikalische und Theoretische Chemie, Universität Tübingen, 72076 Tübingen, Germany*
[12]*Fachbereich Physik, Freie Universität Berlin, Arnimallee 14, D-14195 Berlin, Germany*

The Auger decay of the spin-orbit and molecular-field split Br $3d^{-1}$ core holes in HBr is investigated, both by a photoelectron–Auger-electron coincidence experiment and by *ab initio* calculations based on the one-center approximation. The branching ratios for the Auger decay of the five different core-hole states to the $4p(\sigma,\pi)^{-2}$ dicationic final states are determined. Experimental and theoretical data are in good agreement and conform to results for the $4p\pi^{-2}$ final states from a previous analysis of the high-resolution conventional Auger-electron spectrum. The branching ratios for the Br $3d^{-1}$ Auger decay to the $4p(\sigma,\pi)^{-2}$ with Σ symmetry follow the propensity rule of $L_{2,3}VV$ Auger decay [S. Svensson, A. Ausmees, S. J. Osborne, G. Bray, F. Gel'mukhanov, H. Ågren, A. Naves de Brito, O.-P. Sairanen, A. Kivimäki, E. Nõmmiste, H. Aksela, and S. Aksela, Phys. Rev. Lett. **72**, 3021 (1994)] stating that the oriented core holes decay preferentially by involving a valence electron from an orbital with the same spatial orientation. For the $M_{4,5}VV$ decay in HBr this propensity rule has to be supplemented by the requirement that the Auger-electron channel and the other valence orbital have the same preferential orientation. We also probe the influence of the Auger kinetic energy on the distortion of the photoline caused by the postcollision interaction effect. For small kinetic energies, differences between experimental results and theoretical predictions are identified.

I. INTRODUCTION

In the first approximation, molecular inner-shell orbitals can be described by those of the corresponding isolated atom. That is why one refers for instance to the "Br $3d$ orbital" of the HBr molecule. However, weak but clear molecular effects have been revealed with the advent of high-resolution measurements, such as chemical shifts [1], the presence of vibrational structure [2], gerade and ungerade splitting of core levels in molecules with inversion symmetry [3], molecular dissociation [4], and core-level splitting induced by the molecular field. This latter effect was first detected in the iodine $4d^{-1}$ photoelectron spectra of a series of iodine-containing molecules [5] where the degeneracy of the I $4d_{5/2}^{-1}$ and I $4d_{3/2}^{-1}$ spin-orbit components is lifted by the molecular field, giving rise to three and two molecular inner-shell states, respectively.

Svensson *et al.* discovered in their investigation of the S $2p^{-1}$ holes in H_2S that low-resolution photoelectron and Auger-electron spectra appear to show different values for the spin-orbit splitting [6]. Further investigation revealed that Auger decay rates vary significantly with the different molecular-field split components [7], giving rise to the observed differences. The selectivity on the $2p^{-1}$ initial state was explained by Gel'mukhanov *et al.* with a propensity rule [8] which states that the Auger process proceeds preferentially if the core hole and the valence orbitals involved in the decay have the same orientation. Later on the "Svensson rule" was generalized to $L_{2,3}VV$ Auger decay [9,10], showing that it proceeds with 95% preference if the angular parts of the core hole and one of the involved valence orbitals are identical. Subsequent studies on H_2S investigated this behavior in more detail, both by experiments and theory [11–13]. Since this pioneering work by Svensson *et al.* [7] the Auger decay of molecular-field split states has been studied in a number of additional molecules, including Cl_2 [14], OCS [15,10], CS_2 [16], as well as the hydrogen halides HCl [9,17] and HBr [18]. As will be discussed in more detail further below, the $3d^{-1}$ Auger decay of HBr resembles the behavior found by Svensson *et al.* [7] in several but not all transitions, which motivated the present investigation.

*reinhold.fink@uni-tuebingen.de, pascal.lablanquie@upmc.fr, and puettner@zedat.fu-berlin.de

TABLE I. Expansion coefficients of the HBr valence molecular orbitals in terms of the bromine $4s$ and $4p$ orbitals as well as the hydrogen $1s$ atomic orbital which is not orthogonal to the bromine orbitals. As a consequence, the sum of the squares of the expansion coefficients for the molecular orbitals $4s\sigma$ and $4p\sigma$ is not equal to unity.

	$4s\sigma$	$4p\sigma$	$4p\pi$
Br $4s$	-0.904	0.401	0.000
Br $4p\sigma$	0.067	0.679	0.000
Br $4p\pi$	0.000	0.000	1.000
H $1s$	0.179	0.466	0.000

The molecule HBr has the same number of electrons as the Kr atom and possesses the electronic ground-state configuration $1s^2 2s^2 2p^6 3s^2 3p^6 3d^{10} 4s\sigma^2 4p\sigma^2 4p\pi^4$. Here, the atomiclike inner-shell orbitals are localized on the Br atom. Moreover, the $4p\pi$ molecular valence orbitals are formed by Br $4p$ atomic orbitals while the molecular orbitals labeled as $4s\sigma$ and $4p\sigma$ can be represented to a good approximation by linear combinations of the H $1s$ as well as Br $4s$ and $4p$ atomic orbitals, respectively, as described in Table I. The extraction of two electrons from the nonbonding $4p\pi$ orbital generates the three metastable electronic states $^3\Sigma^-$, $^1\Delta$, and $^1\Sigma^+$ which support vibrational levels. These levels were observed experimentally in the Br $3d^{-1}$ Auger spectra [18,19] and in the double ionization using the electron-electron coincidence method and a magnetic bottle spectrometer. The latter experiments were performed by Eland [20] using He II radiation. Finally, Alagia *et al.* [21] observed these vibrational states by measuring two threshold electrons in coincidence. The corresponding potential curves were calculated by Matila *et al.* [22]. The molecular-field splitting of the Br $3d^{-1}$ core holes was resolved in photoelectron spectra [23–25] which also give access to their lifetime broadening [26].

The high-resolution spectrum of the $3d^{-1} \rightarrow 4p\pi^{-2}$ Auger transitions to the metastable final states $^3\Sigma^-$, $^1\Delta$, and $^1\Sigma^+$ revealed a selectivity of the Auger rates from the molecular-field split core-hole states. However, for one of the Auger decays, namely, $3d^{-1} \rightarrow 4p\pi^{-2}\,^1\Delta$, significant deviations from the above-mentioned Svensson propensity rule were observed [18]. This observation was based on a detailed fit analysis that allows one to obtain the potential-energy curves of the final states as well as the core-hole dependent branching ratios of the Auger rates of the different $3d^{-1} \rightarrow 4p\pi^{-2}$ Auger transitions. This approach includes the description of the vibrational structure of the excitation and the decay process based on the potential-energy curves involved. It also takes into account vibrational lifetime interference, which arises from the overlap of vibrational levels in the intermediate $3d^{-1}$ core-hole state, due to the lifetime broadening.

In the present investigation we used a photoelectron–Auger-electron coincidence method. As demonstrated by Eland *et al.* [13] for H_2S, this method allows one to derive directly the Auger spectra of each individual spin-orbit and molecular-field split core hole. This is the major advantage compared to conventional noncoincidence Auger spectra where such contributions overlap, rendering their identification and comparison

with calculations difficult. Alternative experimental methods have been used, such as measuring Auger spectra at a photon energy where only part of the core-hole components can be populated [14], but the result is not as clear and direct as in the present coincidence method.

As a result of this major advantage, the coincidence data provide directly the branching rations for the Auger decay of the different core-hole states to a given final state, i.e., contrary to Ref. [18] no vibrational progressions have to be analyzed. As consequences, the coincidence method does not require high experimental resolutions and, more importantly, allows us to obtain the branching ratios for decays to dissociative final states.

In the present paper, we measured for the different $3d^{-1} \rightarrow$ v^{-2} ($v = 4s\sigma$, $4p\sigma$, $4p\pi$) Auger transitions the intensity ratios for the spin-orbit and molecular-field split components of the core hole. These conclusions fully confirm the results of Ref. [18] and are in agreement with our theoretical predictions. We show that the intensity ratios for HBr can be qualitatively explained in the frame of the well-established Svensson propensity rule, in combination with a second propensity rule.

II. EXPERIMENT AND FIT ANALYSIS

The photoelectron–Auger-electron coincident spectra were recorded at the undulator beam line U56/2 PGM2 [27] of the BESSY-II synchrotron radiation facility in Berlin, Germany. The single-bunch operation mode of the synchrotron radiation source provided light pulses every 800.5 ns. A mechanical asynchronous chopper, based on a modified turbomolecular pump [28], was used to select one light pulse every $\sim$12.5 μs. The experimental setup consists of a 2-m-long magnetic-bottle multielectron coincidence spectrometer [20], named HER-MES (High Energy Resolution Multi Electron Spectrometer), which has been described elsewhere [29,30]. The conversion from electron time of flights to kinetic energies was obtained by measuring Helium photoelectron spectra at different photon energies and known Auger transitions in rare gases. The energy resolution of the apparatus $\Delta E/E$ is estimated to be $\sim$1.6%.

The coincidence data were accumulated with an electron count rate of about 3 kHz in order to minimize random coincidences. Figure 1(c) shows the energy-correlation map between the $3d^{-1}$ photoelectron (b) and the Auger spectrum (a). The Auger spectrum displayed at the top compares well with those of Wannberg *et al.* [19] and Püttner *et al.* [18] except for a lower resolution that prevents an observation of the vibrational structure in the Auger energy range of 41–46 eV. The photoelectron spectrum in Fig. 1(b) shows the dominant $3d_{3/2}^{-1}/3d_{5/2}^{-1}$ spin-orbit splitting as well as the smaller molecular-field splitting resulting in five components labeled $3d_{j,m_j}^{-1}$ (see Fig. 2).

Since the present time-of-flight technique requires slow photoelectrons to obtain an energy resolution that allows the observation of the molecular-field splitting of the Br $3d^{-1}$ states, a photon energy of 81 eV was selected. This results in slow photoelectrons of 2.5 to 4 eV kinetic energy and, consequently, in very strong postcollision interaction (PCI) effects [31,32]. The PCI effect causes an asymmetry of the photoelectron lines including a tail at the low kinetic-energy side [see Fig. 1(b)]. Similar effects on the high kinetic-energy
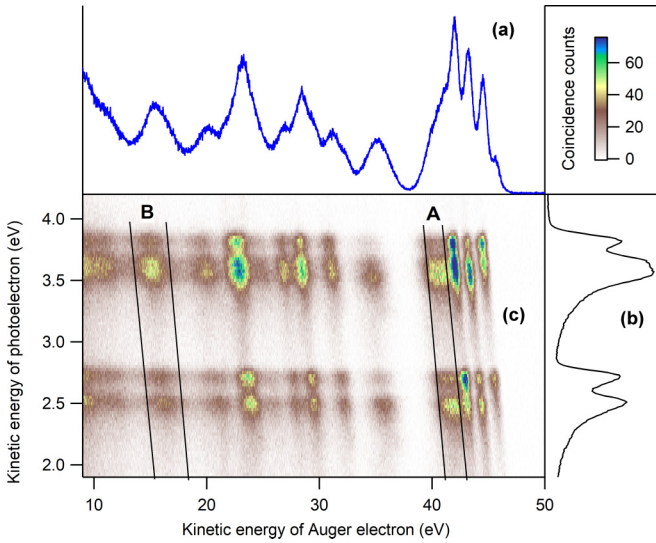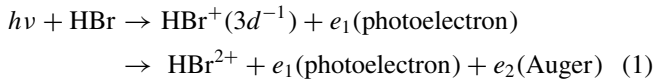
FIG. 1. Energy correlation between photoelectrons and Auger electrons, measured at a photon energy of $h\nu = 81$ eV. Panel (c) displays the two-dimensional coincidence map between the $3d^{-1}$ photoelectrons and the Auger electrons. Panels (a) on the top and (b) on the right side show the resulting Auger-electron and $3d^{-1}$ photoelectron spectra, respectively. The diagonal lines show the different HBr^{2+} final states, and zones A and B indicate the final states selected for the PCI analysis presented in Fig. 2.

sides of the Auger lines are masked in the present experiment by the lower energy resolution.

The two-dimensional plot of Fig. 1(c) exhibits diagonal lines which possess constant sums of the kinetic energies of the two coincident electrons and correspond to the individual HBr^{2+} final states. This can readily be seen by considering the entire process

$$h\nu + \text{HBr} \rightarrow \text{HBr}^+(3d^{-1}) + e_1(\text{photoelectron})$$
$$\rightarrow \text{HBr}^{2+} + e_1(\text{photoelectron}) + e_2(\text{Auger}) \quad (1)$$

as well as the energy conservation between the initial and final state, namely,

$$E_{\text{Auger}} + E_{\text{Photoel}} = h\nu - E_f \quad (2)$$

where E_f is the binding energy of the HBr^{2+} final state. Integration along the diagonal lines in Fig. 1(c) leads to the spectrum in Fig. 3 that displays the population of the different HBr^{2+} final states by the Br $3d^{-1}$ Auger decay. At binding energies below 36 eV (see upper axis), this spectrum shows the three $4p\pi^{-2}$ states $^3\Sigma^-$, $^1\Delta$, and $^1\Sigma^+$. The two overlapping bands at energies around 38 eV are associated to the states $4p\sigma^{-1}4p\pi^{-1}\,^3\Pi$ and $^1\Pi$. The band at ≈ 42.9 eV binding energy is assigned to the $4p\sigma^{-2}\,^1\Sigma^+$ state, while the bands at higher binding energies correspond to excited configurations involving a hole in the deeper $4s\sigma$ valence shell and/or satellite states due to electron correlation. These highly excited HBr^{2+} states were commented upon in Ref. [29] and those with binding energies above 65 eV may decay by autoionization.
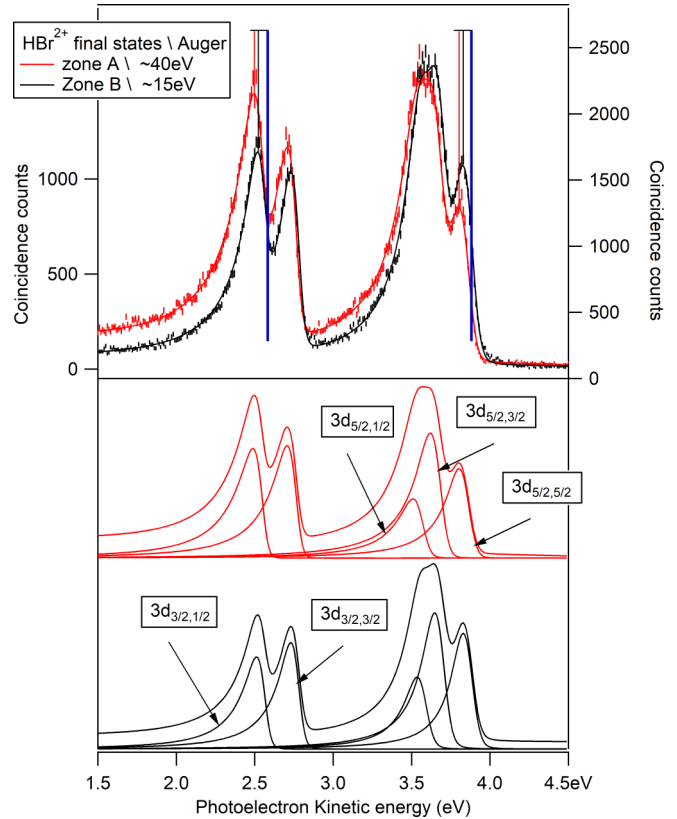

FIG. 2. PCI distortion of the Br $3d^{-1}$ photoelectron lines. The upper panel shows the $3d^{-1}$ photoelectron lines measured in coincidence with Auger electrons in given kinetic-energy ranges so that well-defined final states of HBr^{2+} are populated. The red curves represent data in coincidence with Auger electrons from zone A in Fig. 3, corresponding to an Auger electron of ≈ 40 eV and the final state $4p\sigma^{-1}4p\pi^{-1}(^{1,3}\Pi)$. The black curves are related to zone B, i.e., Auger electrons of ≈ 15 eV leading to highly excited states of HBr^{2+}. The experimental error bars represent only the statistical uncertainties. The solid lines represent the result of a fit analysis taking into account the PCI distortion (see text). The vertical bars mark the positions of the maxima of the PCI-distorted $3d_{3/2,1/2}^{-1}$ and $3d_{5/2,5/2}^{-1}$ photoelectron lines, and their expected position in the absence of PCI effect (broad blue vertical line). The lower two panels give the individual PCI distorted contributions deduced from these fits.

The intensity profile along each diagonal line of Fig. 1(c) shows the population probability of one HBr^{2+} final state by the five $3d^{-1}$ intermediate states. Two such examples are shown in Fig. 2; they are defined in Figs. 1 and 3 by the zones A and B. Zone A with binding energies 36–40 eV, i.e., Auger energies of ≈ 40 eV, covers the states $4p\sigma^{-1}4p\pi^{-1}\,^3\Pi$ and $^1\Pi$, while zone B with binding energies of 60−65 eV and consequently Auger energies of ≈ 15 eV is associated with a band of highly excited HBr^{2+} states. Each spectrum of Fig. 2 reveals in detail five photoelectron lines with considerable shape asymmetries due to the PCI effect.

In order to retrieve the relative intensities of the five core-hole states, these curves have been fitted with the SPANCF curve fitting package, as presented in Refs. [33,34], which takes into account PCI distortion and has been developed by Kukk. As ingredients for the fit, we used the binding energies of the Br
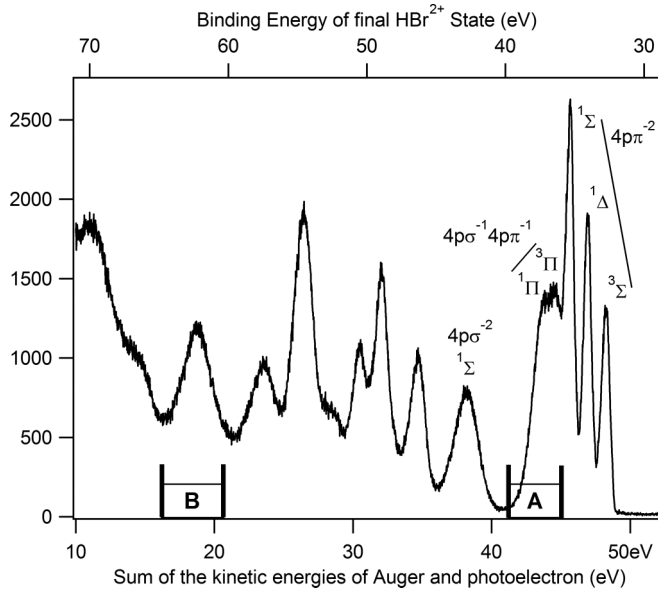
FIG. 3. HBr^{2+} final states populated by Br $3d^{-1}$ Auger decay. The spectrum is obtained from the sum of kinetic energies of Auger electrons, E_{Auger}, and photoelectrons, E_{Photoel}, as indicated on the lower x axis; this corresponds to integrations along the diagonal lines in Fig. 1. The upper x axis displays the binding energy of the final states. Zones A and B indicate the final states selected for the PCI analysis of Fig. 2.

$3d^{-1}$ states from Hu *et al.* [25] and their lifetime widths Γ from Matila *et al.* [26]. The fitting procedure uses PCI profiles in the analytical forms presented by van der Straten *et al.* [32]. The PCI effect shifts the maximum of the photoelectron peaks to lower energies [31,32]. The exact amount of this shift depends on the kinetic energies of both the photoelectron and the Auger electron, as well as the lifetime broadening, as given by the analytical expression [31,35]. For the fitting of each spectrum shown in Fig. 2, only eight free parameters were used: a linear background, the intensities of the five photoelectron peaks, and the energy position of only one of them, namely, the $3d_{5/2,5/2}{}^{-1}$ core-hole state (as the positions of the other peaks are given by the PCI theory and the known binding energies). In order to take into account the experimental resolution, the theoretical PCI profiles were convoluted with a Gaussian function with a full width at half maximum (FWHM) W, which was fixed to $W = 75, 69, 67, 45,$ and 40 meV, respectively, for the $3d_{5/2,5/2}{}^{-1}$, $3d_{5/2,3/2}{}^{-1}$, $3d_{5/2,1/2}{}^{-1}$, $3d_{3/2,3/2}{}^{-1}$, and $3d_{3/2,1/2}{}^{-1}$ components. These values are based on the estimated energy resolution that increases with decreasing kinetic energy of the measured electron. Note that in literature weak vibrational contributions have been observed for the intermediate Br $3d^{-1}$ molecular states [18,26]; they were, however, neglected in the present analysis since they did not improve the quality of the fit result.

The results of the fit analysis reproduce remarkably well the differences of the photoelectron spectra that correspond to the HBr^{2+} final states of zones A and B, which are indicated in Fig. 2 with red and black lines, respectively. In detail, the
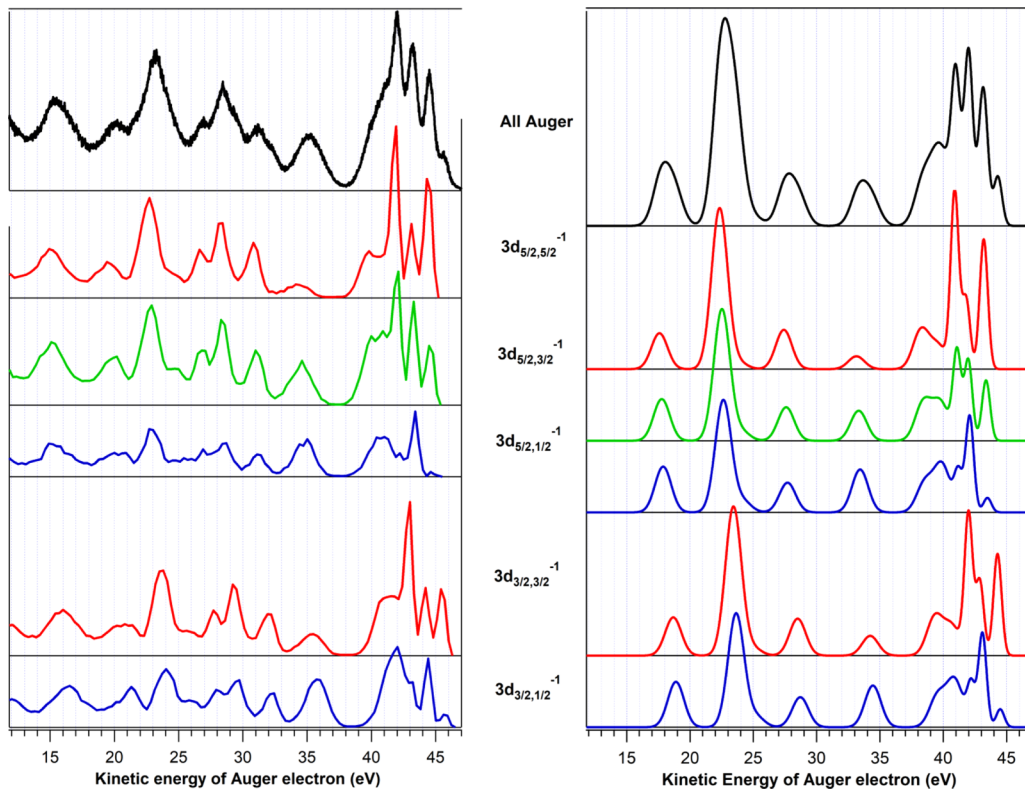

FIG. 4. Total Auger spectrum (top) and its decomposition into the individual Auger spectra of each Br $3d^{-1}$ component. The left panel displays the experimental results obtained from the fit analysis of the diagonal lines in Fig. 1(c) and the right panel displays the present theoretical results. For details, see text.

shifts of the peak maxima and the asymmetry of the profiles are slightly larger for the states in zone A ($E_{\text{Auger}} \approx 40$ eV) than those in zone B ($E_{\text{Auger}} \approx 15$ eV) due to the higher Auger-electron energy in zone A. However, the main result of the fit analysis is the branching ratio for the population of a given HBr^{2+} state by the five different $3d^{-1}$ intermediate core-hole states.

Identical analyses were performed along the entire binding-energy scale of the HBr^{2+} final states shown in Fig. 3; for this purpose, the map in Fig. 1(c) was divided in 130 diagonal stripes with widths of 0.3 eV each to ensure sufficient statistics in the resulting experimental curves. The fit results of these 130 spectra are presented in two different ways. First, the total Auger spectrum [Fig. 1(a)] is decomposed into the individual Auger spectra for the five Br $3d^{-1}$ core holes; these results are presented in the left panel of Fig. 4. Second, the branching ratios for the population of the HBr^{2+} final states via the five Br $3d^{-1}$ intermediate states are presented in Fig. 5 since this presentation is well suited to investigate the propensity rules for spin-orbit and molecular-field split core-hole states.
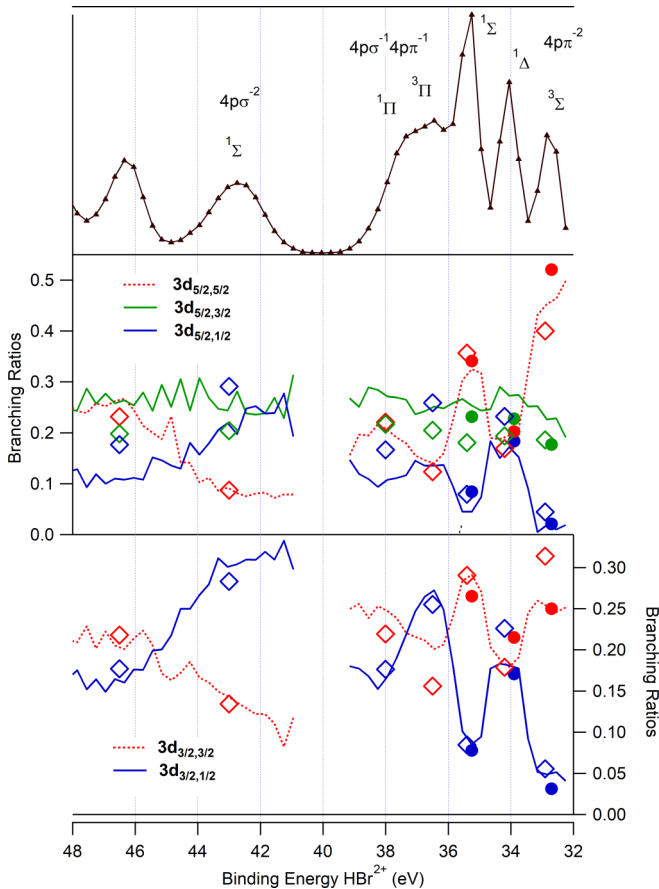

FIG. 5. The lower and the middle panels show the branching ratios for the population of the HBr^{2+} states via the decays of the different $3d_{3/2}^{-1}$ and $3d_{5/2}^{-1}$ components, respectively. The lines are obtained from the fit analysis of the diagonal lines in Fig. 1(c) (see text). The solid dots represent experimental values of Ref. [18] and the open squares represent those of the present calculation. The top panel is a detail of Fig. 3 and represents the population of the HBr^{2+} final states by the $3d^{-1}$ Auger decay.

III. THEORY

Fully theoretical counterparts to the experimental Auger-electron spectra were obtained with an approach following the ideas and methods described in detail in Refs. [9,10,14,36]. The one-center approximation used here allows us to interpret and to generalize the results [10] and makes the methods applicable for a large variety of systems like open-shell and/or polyatomic molecules [36–39]. However, it uses an approximate description in particular for the Auger continuum channel and it is not clear whether this is appropriate for the rather low kinetic energies of the Auger electrons investigated here.

The $3d^{-1}$ core-hole states in the spin-orbit and molecular-field split core-hole states were described with the model Hamiltonian of Johnson *et al.* [24] (see the Appendix for further details). Fitting the model Hamiltonian parameters to the experimental core ionized energy levels from Hu *et al.* [25] (see Table II) gave rise to the population densities and energies of the $3d\lambda$ ($\lambda = \sigma, \pi, \delta$) hole configurations in the $3d_{j,m_j}^{-1}$ states which are also collected in Table II. All calculations used the experimental bond distance (1.4144 Å [40]) as well as the ground-state Hartree-Fock orbitals obtained with the cc-pVTZ basis [41,42]. Nonrelativistic energies were calculated with the configuration interaction method using all two-hole configurations. The corresponding wave functions represent the bound part of the final electronic wave functions used in the one-center approximation to determine Auger decay rates [43–45]. Here each molecular orbital (MO) is approximated by the linear combination of the 1s hydrogen and 1–4s, 2–4p, and 3d bromine atomic orbitals, which provides the best fit to the charge density of the MO as described in Ref. [45]. The MO expansions shown in Table I indicate that the $4s\sigma$ MO is strongly dominated by the Br 4s atomic orbital (AO) with a small contribution of the hydrogen 1s AO while the $4p\sigma$ MO is a strong mixture of all these AOs. Finally, the $4p\pi$ MO has exclusively Br 4p character.

In the one-center approximation, the Auger transition rate is evaluated exclusively from the contributions of the bound bromine AOs, ψ, and the atomic continuum channel ε^{lm} (with the angular and magnetic quantum numbers l and m) to the two-electron Slater integrals

$$\langle c\varepsilon^{lm} \mid vv' \rangle = \iint \psi_c^*(r_1)\varepsilon^{lm*}(r_2)\frac{1}{r_{12}}\psi_v(r_1)\psi_{v'}(r_2)dr_1dr_2 \tag{3}$$

for the core, c, and valence, v and v', orbitals. These integrals were obtained as follows: The RATIP program [46], which has been used widely for Auger and photoionization calculations [47], was employed to calculate the bound wave functions using the Hartree-Dirac-Fock (HDF) approach. Continuum spinors are solved within a spherical but level-dependent potential of the final ion by including the exchange interaction of the emitted electron with the bound-state density. To obtain the nonrelativistic Slater integrals in Eq. (3), the nlj orbital contributions with $j = l \pm 1/2$ were averaged weighted by their degeneracies as described in Ref. [48]. Tests on the Slater integrals for the KLL Auger spectrum of atomic neon show good agreement within 5–10% with the tabulated values by Chen *et al.* [49] which were successfully applied previously to molecular Auger decay [48,50,36,45]. In the HDF approach

TABLE II. Computed partial Auger transition rates (in μa.u.) for the decay of the different spin-orbit and molecular-field split $3d_{j,m_j}^{-1}$ intermediate core-hole states, i, of HBr$^+$ to the final states f of HBr^{2+} with the configurations $(4s\sigma 4p\sigma 4p\pi)^{-2}$. The Auger rates for the nonrelativistic counterparts $3d\lambda^{-1}$ ($\lambda = \sigma$, π, δ) of the $3d^{-1}$ core-hole states are also given. The weights, w, of the nonrelativistic components $3d\lambda^{-1}$ to the $3d_{j,m_j}^{-1}$ intermediate states, the calculated binding energies of the intermediate and final states (E_i and E_f), as well as the leading configurations of the final states are also given.

		i	$3d_{5/2,5/2}^{-1}$	$3d_{5/2,3/2}^{-1}$	$3d_{5/2,1/2}^{-1}$	$3d_{3/2,3/2}^{-1}$	$3d_{3/2,1/2}^{-1}$	$3d\sigma^{-1}$	$3d\pi^{-1}$	$3d\delta^{-1}$
		$w(3d\sigma^{-1}, i)$	0.00	0.00	0.56	0.00	0.44	1	0	0
		$w(3d\pi^{-1}, i)$	0.00	0.71	0.44	0.29	0.56	0	1	0
		$w(3d\delta^{-1}, i)$	1.00	0.29	0.00	0.71	0.00	0	0	1
		E_i	77.17	77.35	77.46	78.26	78.47	77.91	77.82	77.58
f		E_f								
$^3\Sigma^-$	$(4p\pi^{-2})$	33.98	2283	1063	254	1791	317	0	571	2283
$^1\Delta$	$(4p\pi^{-2})$	35.38	1231	1412	1692	1304	1650	1857	1485	1231
$^1\Sigma^+$	$(4p\pi^{-2})$	36.27	3095	1533	674	2465	719	490	904	3095
$^3\Pi$	$(4p\sigma^{-1}4p\pi^{-1})$	37.56	792	1316	1663	1003	1636	1771	1527	792
$^1\Pi$	$(4p\sigma^{-1}4p\pi^{-1})$	38.92	1375	1352	1038	1366	1099	794	1343	1375
$^1\Sigma^+$	$(4p\sigma^{-2})$	44.03	451	1056	1506	695	1465	1670	1300	451
$^3\Pi$	$(4s\sigma^{-1}4p\pi^{-1})$	49.76	1381	1179	1045	1299	1055	1003	1098	1381
$^3\Sigma^+$	$(4s\sigma^{-1}4p\sigma^{-1})$	53.24	199	303	372	241	366	393	345	199
$^1\Pi$	$(4s\sigma^{-1}4p\pi^{-1})$	54.83	5658	4626	3942	5242	3995	3727	4210	5658
$^1\Sigma^+$	$(4s\sigma^{-1}4p\sigma^{-1})$	59.58	1262	1467	1608	1345	1596	1654	1549	1262
$^1\Sigma^+$	$(4s\sigma^{-2})$	70.89	1898	1882	1871	1891	1872	1867	1875	1898

relativistic effects are explicitly considered which might improve the theoretical model. As Br is a mid-Z element, no attempt was made to introduce further relativistic effects in the calculation of the Auger intensities.

Please note that our approach determines the Slater integrals in Eq. (3) from nonrelativistic orbitals. In Ref. [9] symmetry considerations were used to show that the Auger transition rates for the relativistic spin-orbit and molecular-field split core-hole states, $3d_{j,m_j}^{-1}$, to a given final state, f, can be calculated by summing the transition rates of the nonrelativistic hole configurations, $3d\lambda^{-1}$, with the weights, w, of these core-hole configurations in the core-hole state $3d_{j,m_j}^{-1}$, i.e.,

$$I\left(3d_{j,m_j}^{-1} \rightarrow f\right) = \sum_{\lambda=\sigma,\pi,\delta} w\left(3d\lambda^{-1}, 3d_{j,m_j}^{-1}\right) I(3d\lambda^{-1} \rightarrow f).$$

(4)

Thus, the contribution (branching) of the intermediate state on the Auger spectrum, which is the central topic of this paper, can be deduced from the Auger transition rates of the nonrelativistic $3d\lambda^{-1}$ configurations. This was used to calculate the Auger transition rates shown in Table I and it will be used below to rationalize the observed branching of intensity patterns in the HBr Auger-electron spectrum.

IV. RESULTS AND DISCUSSION

A. Deceleration of the $3d^{-1}$ photoelectron caused by the PCI effect

The influence of the PCI effect on the Br $3d^{-1}$ photoelectron lines of HBr has been studied to date by Odling-Smee *et al.* [51]. In their study the photon energy was varied while the influence of the kinetic energy of the individual Auger electron was not taken into account. Instead, their conventional photoelectron spectra contain the superposition of photoelectron lines associated to Auger decays to different final states,

characterized by different energies of the Auger electron. In contrast to this, the present photoelectron–Auger-electron coincidence method allows us to extract photoelectron spectra for well-defined final states and Auger energies and to observe in fine detail the influence of the kinetic energy of the Auger electron on the PCI distortion of the Br $3d^{-1}$ photoelectron lines. In detail, our fit enables us to obtain an experimental estimate of the $3d_{5/2,5/2}^{-1}$ peak position, $E(3d_{5/2.5/2})$, as a function of the kinetic energy of its associated Auger electron. The PCI shift $\Delta(3d_{5/2,5/2})$ is then defined by

$$\Delta(3d_{5/2,5/2}) = E(3d_{5/2,5/2}) - E^0(3d_{5/2,5/2})$$
$$= E(3d_{5/2,5/2}) - [h\nu - E_i(3d_{5/2,5/2})]. \quad (5)$$

Here, $E^0(3d_{5/2,5/2})$ is the kinetic energy of the $3d_{5/2,5/2}^{-1}$ peak in the absence of the PCI effect, which is derived from the photon energy $h\nu$ and the binding energy $E_i(3d_{5/2,5/2})$ taken from Hu *et al.* [25]. The PCI shift $\Delta(3d_{5/2,5/2})$ derived from the fit analysis is shown in Fig. 6 as a function of the Auger energy.

We recall that the PCI shifts of the other $3d^{-1}$ components were automatically reproduced by the SPANCF fitting procedure, and that it is only the position of the $3d_{5/2,5/2}^{-1}$ component which is a free parameter of the fit. It is well known that the PCI distortion and the photoelectron deceleration are stronger for faster Auger electrons. We confirm this trend for the PCI shift $\Delta(3d_{5/2,5/2})$ in Fig. 6, in this particular case for a photoelectron with a kinetic energy of ≈ 3.8 eV detected in coincidence with an Auger electron with a kinetic energy that varies between 7 and 45 eV. Such dependences for photoelectron lines with well-defined kinetic energy of the Auger electron were experimentally observed before for the Xe atom (a $4d_{5/2}^{-1}$ photoelectron of ≈ 2.6 eV kinetic energy and Auger energies in the 8–30-eV range [52]) and for the GeCl$_4$ molecule (a $3d_{5/2}^{-1}$ electron of ≈ 0.9 eV kinetic energy and Auger energies in the 0−12-eV range [53]). However, the
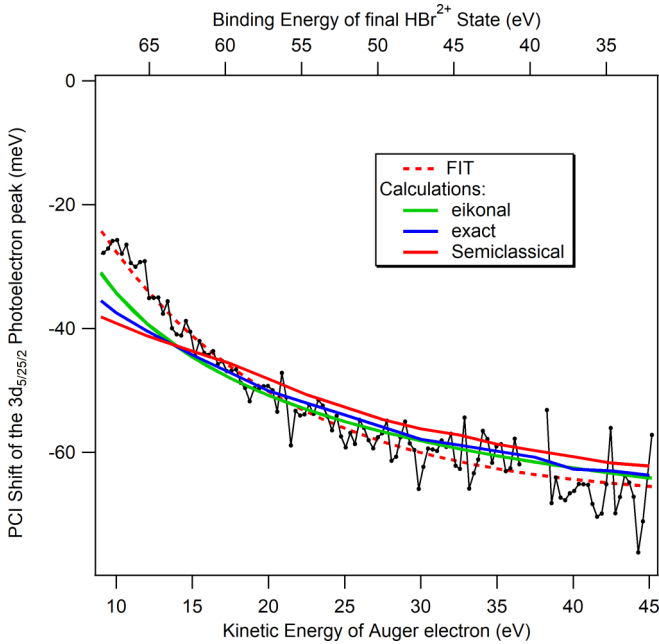
FIG. 6. PCI shift for the $3d_{5/2,5/2}^{-1}$ photoline as a function of the Auger kinetic energy. The black dots are experimental values obtained from the fit (see text). The red dotted line is a fitted curve to guide the eye. The solid lines give the PCI dependence predicted by three different models, namely, eikonal approximation [31], semiclassical approximation [32], and eikonal approximation with an exact account of Auger-electron–photoelectron interaction [54]. The absolute experimental energy error bar is estimated as ± 30 meV. Scatter of the data points suggests that the relative error bar is smaller at ± 3 meV. Photon energy used in the theoretical estimation was set at 81.05 eV. For details, see text.

present results for HBr are more precise than in the previous investigations. For $\Delta(3d_{5/2,5/2})$ we estimate the absolute error bars to ± 30 meV due to the uncertainties in the photon energy, the electron energy calibration, and the $3d_{5/2,5/2}^{-1}$ binding energy [25]. Contrary to this, the relative error bars are much smaller, within ± 3 meV, as can be seen by the scattering of the data points in Fig. 6.

In order to analyze the results in more detail we have calculated the PCI shift within three different models, namely, the eikonal approximation [31], the semiclassical approximation [32], and the eikonal approximation with exact account of Auger-electron–photoelectron interaction [54]. All these models predict an angular dependent PCI distortion of the photoelectron line shape. Since our measurements do not depend on the relative angle between the emission of the Auger electron and the photoelectron we have to average the calculated shapes over this relative angle. Moreover the eikonal approximation [31] allows us to obtain easily the analytical expression for the PCI shift:

$$\Delta \varepsilon = \Gamma \left(1/V_{\text{photo}} - 1/|\vec{V}_{\text{photo}} - \vec{V}_{\text{Auger}}| \right)/2 \qquad (6)$$

where Γ is the inner vacancy width and $\vec{V}_{\text{photo}}$ and $\vec{V}_{\text{Auger}}$ are the velocities of the photoelectron and Auger electron, respectively. After averaging over the angle of the Auger-electron

emission this expression is reduced to

$$\Delta = \overline{\Delta \varepsilon} = \Gamma \left(1/V_{\text{photo}} - 1/V_{\text{Auger}} \right)/2. \qquad (7)$$

The same result has been obtained by Armen *et al.* [35]. The first term in the parentheses of this expression is associated with the interaction between the photoelectron and the receding ion whereas the second one reflects the interaction between the photoelectron and the Auger electron. These interactions have opposite influence on the photoelectron propagation and, hence, have opposite signs in the expressions for $\Delta \varepsilon$. In the case of a deep inner vacancy decay, the velocity of the Auger electron is much larger than the velocity of the photoelectron and the second term has little influence on the PCI shift. However, in our case the velocity of the Auger electron is comparable with the velocity of the photoelectron and the interaction between the emitted electrons affects remarkably the PCI shift.

In Fig. 6 we present calculated PCI shifts averaged over the relative angle emission. The PCI shifts calculated within the eikonal approximation [31], the semiclassical approximation [32], and the eikonal approximation with exact account of Auger-electron–photoelectron interaction [54] are shown by green, red, and blue lines, respectively. As a parameter of calculation, we use the value of 97 meV for the inner vacancy width [26]. It can be observed that in the region of the Auger-electron energies $E_{\text{Auger}} > 15$ eV all the models describe adequately the measured shift. However, for smaller energies, namely, $E_{\text{Auger}} < 15$ eV, the measured dependence (dotted red line) has a larger slope and smaller absolute values than those expected from the calculation. The reason of such disagreement might be due to the procedure of the angular averaging. Our calculation takes into account the angular dependent PCI distortion factor only and neglects the angular dependence of the Auger electrons. In other words, for the sake of simplicity and due to lack of more detailed information, the employed PCI models assume that the Auger electrons have isotropic distributions while carrying out the averaging of the PCI distorted line shape over the angle of the Auger electron. Actually, it was shown that for molecules Auger electrons associated with different dicationic final states can have strongly anisotropic distributions [50,55] and, consequently, contribute differently during integration over the phase volume. This effect is mostly remarked for similar velocities of the emitted electrons, i.e., for the region $E_{\text{Auger}} < 12$ eV. Another reason for the observed disagreement may originate from the fact that in this case highly excited HBr^{2+} final states are populated, which may release a second-step Auger electron as some of the authors of this paper demonstrated in Ref. [29]: the presence of this second low-energy Auger or autoionization electron may affect PCI.

B. Filtering of Auger spectra associated with the decay of each $3d^{-1}$ molecular intermediate state

The left panel of Fig. 4 displays the experimental Auger spectra of the different Br $3d^{-1}$ states, which are deduced from the fit analysis presented in the experimental chapter. For comparison, the corresponding theoretical spectra based on the Auger rates and transition energies presented in Table II are shown in the right panel. The transitions to the metastable final states $4p\pi^{-2}\,^3\Sigma^-$, $^1\Delta$, and $^1\Sigma^+$ are represented by Gaussians

functions of 0.75 eV FWHM in order to simulate the vibrational progressions observed in Ref. [18]. For all other HBr^{2+} final states, Gaussians with a width of 1.5 eV FWHM are used since they are expected to be strongly dissociative. The agreement between the experimental and theoretical partial Auger spectra is quite good, especially for Auger kinetic energies above ≈ 33 eV corresponding to the HBr^{2+} final states of the configurations $4p\pi^{-2}$, $4p\pi^{-1}4p\sigma^{-1}$, and $4p\sigma^{-2}$. The relative intensities of the three transitions with the highest kinetic energies, namely, the $3d^{-1} \rightarrow 4p\pi^{-2}$ transitions, differ significantly in the various Br $3d^{-1}$ Auger spectra. This clearly demonstrates the selectivity of Auger decay on the orientation of the Br $3d^{-1}$ core hole. In the kinetic-energy range below 33 eV the calculated Auger spectra show less spectral features than in the experimental ones. The additional features in the experiment are due to Auger transitions to three-hole one-particle ($3h$-$1p$) states which have not been included in the calculations. The most intense peak in this zone, found experimentally at ≈ 23 eV, is, however, well reproduced in the calculations, and it is assigned to the $4s\sigma^{-1}4p\pi^{-1}\,^1\Pi$ final state. Its intensity is higher in the calculations than in the experiment, but it is expected that it will be redistributed to the $3h$-$1p$ states once they are taken into account in more sophisticated calculations. This expectation is fully in line with the finding of strong configuration interaction between the configuration $4s\sigma^{-1}$ and low-n ($n = 5, 6$ describing Rydberg orbitals) $4p\pi^{-2}nl\lambda$, as observed in the $4s\sigma^{-1}$ photoelectron spectrum [56]. As a consequence, the $3h$-$1p$ states are suggested to have significant $4p\pi^{-3}nl\lambda$ character.

C. Selectivity of the Auger decay of the $3d^{-1}$ molecular intermediate states: Partial explanation with the Svensson propensity rule

Figure 5 displays the branching ratios extracted for the population of the final states caused by the five different Br $3d^{-1}$ intermediate states. These curves are equal to the ratios of the partial Auger spectra shown in Fig. 4, however plotted on the binding-energy scale. In the top panel of Fig. 5, the total population of the HBr^{2+} final states due to the $3d^{-1}$ Auger decay is reported (see also Fig. 3). The general trend of some of these branching ratios follows the propensity rule discovered by Svensson *et al.* [7] for $L_{2,3}VV$ decay. According to this propensity rule, high Auger rates are expected when the core hole has the same orientation as one of the involved valence orbitals. Please note that, for $L_{2,3}VV$ (i.e., $L_{2,3}MM$) decay, core ($2p$) and valence ($3s$ or $3p$) orbitals obviously have the same "orientation" in, e.g., the $2p_1$–$3p_1$ or $2p_x$–$3p_x$ pairs where the core and valence orbitals have the *same* angular shape. However, in $M_{4,5}VV$ (i.e., $M_{4,5}N_{1,2,3}N_{1,2,3}$) decay of the HBr molecule the ($3d$) core and ($4s$ and $4p$) valence orbitals *never* have the same angular form. Consequently, only their *preferential* orientation with respect to the molecular axis can be considered. This is done in the following in order to investigate whether the Svensson rule can be extended to interpret the branching of the $3d^{-1}$ decay in HBr.

The Br $3d_{j,m_j}^{-1}$ core-hole states can be represented as a linear combination of the nonrelativistic $3d\lambda^{-1}$ eigenstates with $\lambda = \sigma, \pi$, and δ. The weights for this description are given in the upper part of Table II and are in good agreement with previous

results from Johnsson *et al.* [24]. Based on these weights, the molecular Br $3d_{j,m_j}^{-1}$ states can be divided in three groups. The first group consists of the core holes Br $3d_{5/2,5/2}^{-1}$ and Br $3d_{3/2,3/2}^{-1}$ which both have strong $3d\delta$ contributions, i.e., the core holes are oriented fully (Br $3d_{5/2,5/2}^{-1}$) or preferentially (Br $3d_{3/2,3/2}^{-1}$) perpendicular to the HBr internuclear axis. The second group consists of the core holes Br $3d_{5/2,1/2}^{-1}$ and Br $3d_{3/2,1/2}^{-1}$ which both have strong $3d\sigma$ contributions. These contributions lead to a spatial orientation mainly parallel to the HBr internuclear axis. The third group consists of the Br $3d_{5/2,3/2}^{-1}$ core-hole state alone and possesses strong $3d\pi$ contributions. The corresponding $3d\pi$ orbitals exhibit nodes along and perpendicular to the molecular axis so that the highest probability for the core hole is found along a line oriented at $45°$ relative to the axis.

By applying the above-mentioned propensity rule [7] to HBr we result in the simple picture that $3d\delta$ and $3d\sigma$ core holes are predominately filled by $4p\pi$ and $4p\sigma$ valence orbitals, respectively. Consequently, it is expected that the Br $3d_{5/2,5/2}^{-1}$ and Br $3d_{3/2,3/2}^{-1}$ core holes (indicated in Fig. 5 with red dotted lines) decay preferentially by involving two electrons from the $4p\pi$ molecular orbitals since they are also oriented perpendicular to the HBr internuclear axis. This is fully in line with the observed preferential decay of these "red" intermediate states to the $4p\pi^{-2}\,^3\Sigma^-$ and $^1\Sigma^+$ final states. For the core-hole states Br $3d_{5/2,1/2}^{-1}$ and Br $3d_{3/2,1/2}^{-1}$ (indicated in Fig. 5 with blue solid lines) we expect due to the orientation parallel to the internuclear axis a preferential decay to the $4p\sigma^{-2}\,^1\Sigma^+$ final state, which is also in agreement with the experiment. The intermediate state $3d_{5/2,3/2}^{-1}$ (indicated in Fig. 5 with green solid lines) shows no clear orientation with respect to the internuclear axis. Consequently, it has no preferential decay and populates all HBr^{2+} final states with a remarkably constant branching ratio of about 25–30%.

Figure 5 also shows the theoretical ratios derived from Table II (see open squares), and for the three metastable $4p\pi^{-2}$ final states the experimental branching ratios are obtained in Ref. [18] (see solid dots), resulting in a good agreement between all three approaches. From this can be concluded that the final states $4p\pi^{-2}\,^3\Sigma^-$ and $^1\Sigma^+$ as well as $4p\sigma^{-2}\,^1\Sigma^+$ follow the simple propensity rule for the selectivity of the Auger decay of the $3d^{-1}$ intermediate states. However, the Br $3d^{-1}$ Auger transitions to the $4p\pi^{-2}\,^1\Delta$ final state of HBr^{2+} do not obey this simple propensity rule with the expectation of a preferential population by the "red" group of states, namely, Br $3d_{5/2,5/2}^{-1}$ and Br $3d_{3/2,3/2}^{-1}$, in full agreement with the sophisticated fit analysis of the high-resolution Auger spectrum [18].

The propensity rule of Svensson for the $4p\sigma^{-1}4p\pi^{-1}$ final state of HBr^{2+} predict no preferential formation following the decay of the differently oriented intermediate states, because they involve the removal of two valence electrons oriented in different directions. Nevertheless, we observe a weakly selective decay: the $4p\sigma^{-1}4p\pi^{-1}\,^1\Pi$ final state is slightly preferentially populated by the decay of the $3d_{5/2,5/2}^{-1}$ and $3d_{3/2,3/2}^{-1}$ intermediate states of the "red" group, which are mainly perpendicularly oriented. In contrast, the $4p\sigma^{-1}4p\pi^{-1}$ $^3\Pi$ final state is preferentially populated by the decay of the intermediate states $3d_{5/2,1/2}^{-1}$ and $3d_{3/2,1/2}^{-1}$ of the "blue" group, which are mostly parallel oriented.

D. Selectivity of the Auger decay of the $3d^{-1}$ molecular intermediate states understood by an additional propensity rule

The most interesting result for HBr is that the Svensson propensity rule that applies to $L_{2,3}VV$ Auger decay [9] and perfectly explains the branching of, e.g., the HCl Auger transition rates is only partially valid for Auger transitions in HBr. To understand the more complex behavior of HBr, one has to consider several aspects. We shall first present an overview of the main arguments and their important outcomes while more detailed explanation will be given further below.

The central points are the possible combinations for the symmetries $nl\lambda$ of the core hole, the two valence holes, as well as the symmetries $\varepsilon l\lambda$ for the continuum Auger electron. These combinations can be determined from angular momentum and parity conservation due to the symmetry of the Auger operator and are given in Table II. From this consideration we derive two important differences between HCl and HBr.

First, one has to generalize the propensity rules by not only taking the orientation of the core hole and of the valence orbitals into account but also considering the orientation of the second valence orbital and the continuum wave function. This is necessary since HBr shows with respect to these orientation arguments a significantly more complicated behavior than HCl. Most interestingly, for HCl both orientation arguments provide always the same result. This justifies the simplification to take only the orientation argument for the core hole and one valence orbital into account, as introduced by Svensson *et al.* [7].

Second, in the case of HCl the core holes and some of the valence orbitals have p character and thus identical angular shape. In contrast to this, for HBr, the holes in the valence shell have p character while the core hole and the continuum electron have d character. Since the angular dependences of p and d orbitals are different this has an influence on the two-electron integrals in Eq. (3). In particular, the ratio of the two-electron integrals for the favorable to the unfavorable orientation of the involved electrons is larger for HCl than for HBr. Thus, orientation effects are generally less pronounced in the $3d^{-1}$ Auger decay of HBr than in the $2p^{-1}$ Auger decay of HCl.

In the following we shall discuss the arguments in detail. We start with the determination of the allowed symmetries $\varepsilon l\lambda$ of the continuum Auger electron. For this, we consider the Auger decay of HBr and HCl as an atomiclike Auger decay of krypton and argon, respectively, in the presence of a preferential axis. This is equivalent to defining a molecular axis but neglecting the modification of the molecular $4p\sigma$ orbital caused by the H atom. Due to the preferential axis it is reasonable to consider the nonrelativistic atomic wave function of Ar and Kr as molecular wave functions, i.e., $3d\sigma$, $3d\pi$, $3d\delta$, $np\sigma$, and $np\pi$. As already indicated above, the symmetry $\varepsilon l\lambda$ for the Auger electron can be derived based on angular momentum and parity conservation by taking into account the symmetry of the core hole and the valence orbitals as well as the angular momentum coupling of the two valence orbitals. For atomic neon a detailed working example is given by Schmidt [57]. For molecules, the conservation of Λ_z has also to be taken into account since the energy levels $nl\lambda$ do not only depend on nl but also λ.

In detail, we represent the Br $3d^{-1} \rightarrow 4p(\sigma, \pi)^{-2}$ and the Cl $2p^{-1} \rightarrow 3p(\sigma, \pi)^{-2}$ by Kr $3d^{-1} \rightarrow 4p^{-2}$ and Ar $2p^{-1} \rightarrow$ $3p^{-2}$ Auger transition, respectively. For the Kr $3d^{-1} \rightarrow 4p^{-2}$ Auger transitions the outgoing Auger electron can have—based on angular momentum and parity conservation—εs symmetry ($^1D_2$ final state), εd symmetry ($^1S_0$, $^3P_{0,1,2}$, $^1D_2$), and εg symmetry ($^1D_2$) as well as for the Ar $2p^{-1} \rightarrow 3p^{-2}$ Auger transition εf symmetry ($^1D_2$ final state) and εp symmetry ($^1S_0$, $^3P_{0,1,2}$, $^1D_2$). Since the present calculations for HBr show that the εd channel is dominant we focus on this channel for HBr/Kr and the εp channel for HCl/Ar. For the different core-hole states of Br/Kr $3d^{-1}$ and Cl/Ar $2p^{-1}$ as well as $np(\sigma, \pi)^{-2}$ dicationic final states the allowed symmetries $\varepsilon l\lambda$ for the outgoing Auger electron are summarized in Table III.

In the next step we shall discuss the generalization of the propensity rules which can be identified on the basis of the orientation of the orbitals in the two-electron matrix element of Eq. (3) with respect to the molecular axis. For a large two-electron matrix element and, consequently, a large Auger intensity two conditions have to be simultaneously fulfilled.

(1) The core-hole wave function $\psi_c(r_1)$ is oriented in a similar way as the valence orbital $\psi_v(r_1)$ (condition c).

(2) The continuum wave function $\varepsilon^{lm}(r_2)$ and the valence orbital $\psi_{v'}(r_2)$ have similar orientations (condition ε).

Note that condition c is equivalent to the propensity rule of Svensson. In the following, we shall discuss for which symmetry combinations of core holes, valence orbitals, and continuum electron the orientational properties of conditions c and ε are fulfilled. For this purpose, the orientational properties are given in Table III by using the following code: In the case that both orbitals involved in a given condition (c or ε) are preferentially oriented in the same direction, contribution to the Auger transition integral is expected to be strong and it is indicated with "+" (e.g., c+). Moreover, "−" and "0" indicate that the two orbitals are oriented perpendicular and in an angle of 45 deg, respectively, to each other, i.e., in these cases the transition integrals are smaller. Based on this encoding, c+ε+ stands for a fulfillment of both conditions and, as a consequence, for a large Auger matrix element. Contrary to this, c−ε− corresponds to maximal difference in the orientation, i.e., to small Auger matrix elements.

Such encodings for the orientation are given in Table III for all transitions, together with the corresponding calculated Auger rates. Generally, a significant correlation between the intensities and the encoding of the orientation is found. For the final states $4p\pi^{-2}\,^3\Sigma^-$ and $4p\pi^{-2}\,^1\Sigma^+$ a significant decrease of the Auger intensity can be found from the Br $3d\delta^{-1}$ core hole (encoding c + ε+) to Br $3d\pi^{-1}$ (encoding c0ε0) to Br $3d\sigma^{-1}$ (encoding c−ε−). For the final state $4p\sigma^{-2}\,^1\Sigma^+$ a similar behavior can be found, however, from Br $3d\sigma^{-1}$ to Br $3d\pi^{-1}$ to Br $3d\delta^{-1}$, due to the opposite encoding. The less dominant intensity of the c + ε+ encoding in the case of the molecular $4p\sigma^{-2}$ final state as compared to the $4p\pi^{-2}$ final states can be understood by a significant mixing of the atomic Br $4p\sigma$ orbital with the H $1s$ orbital. This lifts the inversion symmetry for this orbital and leads in the calculations to significant contributions of $\varepsilon f\lambda$ for the continuum channel, which is forbidden in the present atomiclike approach. Contrary to this, the $4p\pi$ orbitals can be considered rather atomiclike. For the transitions to all other final states under consideration we do not have transitions with the encodings c+ε+ and c−ε−. As a consequence, the Auger intensities are less dependent on the

TABLE III. Summarized considerations on the properties of the Br $3d^{-1} \to 4p(\sigma, \pi)^{-2}$ Auger transitions of HBr and Cl $2p^{-1} \to 3p(\sigma, \pi)^{-2}$ Auger transitions of HCl. For the different orientations of the $3d^{-1}$ and $2p^{-1}$ core-hole states the allowed symmetries of the $\varepsilon d\lambda$ and $\varepsilon p\lambda$ continuum wave functions, respectively, are given. Moreover, for each transition the orientational match of the wave functions relevant for the Auger matrix element is encoded, as detailed in the text, with an estimate of the c and ε orientations. The calculated Auger rates in 10^{-6} a.u. are also given. Partially lower intensities than those given in Table II are due to the fact that here only the transitions with $\varepsilon d\lambda$ continuum channels are considered.

	Br/Kr $3d\sigma$	Br/Kr $3d\pi$	Br/Kr $3d\delta$	Cl/Ar $2p\sigma$	Cl/Ar $2p\pi$
$np\pi^{-2}(^3\Sigma^-)$	$\varepsilon d\sigma$	$\varepsilon d\pi$	$\varepsilon d\delta$	$\varepsilon p\sigma$	$\varepsilon p\pi$
	c$-\varepsilon-$	c0ε0	c$+\varepsilon+$	c$-\varepsilon-$	c$+\varepsilon+$
	0	571	2283	0	837
$np\pi^{-2}(^1\Delta)$	$\varepsilon d\delta$	$\varepsilon d\pi$	$\varepsilon d\sigma$	$(\varepsilon f\delta)$	$\varepsilon p\pi$
	c$-\varepsilon+$	c0ε0	c$+\varepsilon-$		c$+\varepsilon+$
	1701	1276	851	41	865
$np\pi^{-2}(^1\Sigma^+)$	$\varepsilon d\sigma$	$\varepsilon d\pi$	$\varepsilon d\delta$	$\varepsilon p\sigma$	$\varepsilon p\pi$
	c$-\varepsilon-$	c0ε0	c$+\varepsilon+$	c$-\varepsilon-$	c$+\varepsilon+$
	401	833	3059	18	484
$np\sigma^{-1}np\pi^{-1}(^3\Pi)$	$\varepsilon d\pi$	$\varepsilon d\sigma/\varepsilon d\delta$	$\varepsilon d\pi$	$\varepsilon p\pi$	$\varepsilon p\sigma$
	c$+\varepsilon$0 or c$-\varepsilon$0	c0$\varepsilon+$ or c0$\varepsilon-$	c$+\varepsilon$0 or c$-\varepsilon$0	c$+\varepsilon+$ or c$-\varepsilon-$	c$+\varepsilon+$ or c$-\varepsilon-$
	1581	1318	527	1199	690
$np\sigma^{-1}np\pi^{-1}(^1\Pi)$	$\varepsilon d\pi$	$\varepsilon d\sigma/\varepsilon d\delta$	$\varepsilon d\pi$	$\varepsilon p\pi$	$\varepsilon p\sigma$
	c$+\varepsilon$0 or c$-\varepsilon$0	c0$\varepsilon+$ or c0$\varepsilon-$	c$+\varepsilon$0 or c$-\varepsilon$0	c$+\varepsilon+$ or c$-\varepsilon-$	c$+\varepsilon+$ or c$-\varepsilon-$
	198	693	594	640	403
$np\sigma^{-2}(^1\Sigma^+)$	$\varepsilon d\sigma$	$\varepsilon d\pi$	$\varepsilon d\delta$	$\varepsilon p\sigma$	$\varepsilon p\pi$
	c$+\varepsilon+$	c0ε0	c$-\varepsilon-$	c$+\varepsilon+$	c$-\varepsilon-$
	977	709	162	593	17

orientation of the core hole, in agreement with the observation. This holds in particular also for the Br $3d^{-1} \to 4p\pi^{-2} {}^1\Delta$ transition, for which the violation of the propensity rule c for the core-hole orientation was observed for the first time.

Up to now we considered only the symmetry eigenstates Br $3d\lambda^{-1}$ and Cl $2p\lambda^{-1}$ but not the relativistic eigenstates Br $3d_{j,mj}^{-1}$ and Cl $2p_{j,mj}^{-1}$. However, as discussed above the latter states can be described as linear combinations of $nl\lambda^{-1}$ terms with one leading contribution (see Table II). This allows us to transfer the results for the $nl\lambda^{-1}$ core holes to the nl_{j,m_j}^{-1} core holes.

Finally, we will discuss the Cl $2p^{-1} \to 3p\pi^{-2}$ and Cl $2p^{-1} \to 3p\sigma^{-2}$ Auger transitions in HCl. Most interestingly, here the encoding of the orientation requirements is much simpler, resulting either in c$+\varepsilon+$ or in c$-\varepsilon-$. As a consequence, it is sufficient to consider one of the orientation arguments (see above) as has been done by all previous works by using the orientation argument of the core hole and the valence electrons (condition c). Due to the fact that only the encodings c$+\varepsilon+$ and c$-\varepsilon-$ exist, we expect for all Cl $2p^{-1} \to 3p\pi^{-2}$ Auger transitions a strong dependence of the Auger rate on the core-hole orientation, in agreement with the observation.

In the Appendix we show how the rates for the Br $3d\lambda^{-1} \to 4p\pi^{-2}\varepsilon d\lambda'$ Auger transition are obtained by using the one-center approximation with the dominant d-Auger channels, spherical symmetric orbitals, and a single configuration representation of the $4p\pi^{-2}$ final states. This corresponds to our approach of describing the Br $3d^{-1} \to 4p(\sigma, \pi)^{-2}$ transitions, however in a much more complete manner. The obtained results reproduce the Auger intensity pattern quantitatively and

qualitatively support the extended propensity rule discussed above.

As the final aspect we want to discuss the influence of the angular dependences of the p and d orbitals on the Auger intensity. We already pointed out above that in the case of HCl the $2p^{-1}$ core hole is filled by a $3p$ valence electron. At the same time the second $3p$ valence electron goes to an εp continuum channel. Contrary to this, in case of HBr both $4p$ valence electrons change to d channels, namely, the $3d^{-1}$ hole or the εd continuum channel. Now the Auger transition rates described by the two-electron integrals in Eq. (3) obtain large absolute values if for both electrons the angular parts of the related orbitals are identical. In the $L_{2,3}VV$ Auger decay of HCl this is the case for both valence electrons and the resulting two-electron integrals exceed the size of all others by a factor of more than 3.4. This causes 95% of these Auger transitions to be associated with a decay that is encoded by c$+\varepsilon+$ according to the generalized propensity rules (see Table III). This kind of highly intense decay channel of the $L_{2,3}VV$ transitions is possible for the typically investigated phosphorous, sulphur, chlorine, or argon compounds where electrons occupy the $3p$-type orbitals at the core-hole atom.

For HBr the angular parts of the core and continuum orbitals with d symmetry and the valence orbitals with p symmetry are necessarily different and a similarly strong preference for certain transitions encoded with c$+\varepsilon+$ does not exist. In turn we expect that transitions encoded with c$-\varepsilon-$ are less efficiently suppressed. These considerations are confirmed by the Auger transitions to the final states $n\pi^{-2} {}^1\Sigma^+$ and $n\sigma^{-2} {}^1\Sigma^+$. Both can be populated via a transition encoded by c$+\varepsilon+$

and a transition encoded by $c-\varepsilon-$. For HCl the intensity ratio of the $c+\varepsilon+$ to $c-\varepsilon-$ transition is about 30:1 averaged over both final states while the same ratio for HBr is only about 7:1. From these considerations we conclude that for $M_{4,5}VV$ decay the orientation effects are generally less pronounced than for $L_{2,3}VV$ Auger transitions.

V. CONCLUSIONS

We have studied the Auger decay of the spin-orbit and molecular-field split Br $3d^{-1}$ core hole of HBr by using *ab initio* calculations and a photoelectron–Auger-electron coincidence experiment. The present coincidence method confirms for the metastable HBr^{2+} final states $4p\pi^{-2}\,{}^3\Sigma^-$, ${}^1\Delta$, and ${}^1\Sigma^+$ the intensity Auger ratios for the five different Br $3d^{-1}$ components deduced from the analysis of a conventional high-resolution Auger spectrum [18]. However, this experimental approach is not limited to metastable states, but also allows studies on the intensity ratios of dissociative final states.

A large part of the final states exhibits a selectivity of the Auger rate on the core-hole orientation, which is in line with the propensity rule discovered for the $L_{2,3}VV$ Auger decay by Svensson *et al.* [7]: The core-hole states oriented mainly perpendicular to the HBr axis decay preferentially to the $4p\pi^{-2}\,{}^3\Sigma^-$ and ${}^1\Sigma^+$ final states, due to the perpendicular orientation of the $4p\pi$ valence electrons, while the core-hole states oriented mainly parallel to the HBr axis decay preferentially to the $4p\sigma^{-2}\,{}^1\Sigma^+$ final state. However, the Auger decays to the $4p\pi^{-2}\,{}^1\Delta$ final state show no strong dependence on the core-hole orientation in contrast to the prediction of this propensity rule.

This behavior and all observed intensity patterns are well reproduced by our calculations, which are based on the one-center approximation for the Auger decay. This shows that the one-center approximation is still applicable for this type of Auger decay with kinetic energies below 50 eV. An analysis of the intensity calculations demonstrates that a second propensity rule has to be considered, in addition to the well-established Svensson one. Namely, Auger transitions are intense if the orientations of the core hole and of one of the valence orbitals are similar (Svensson rule) and if, in addition, the orientations of the continuum wave function of the Auger electron and the other valence orbital match as well. We show that these propensity rules are redundant in the case of $2p^{-1}$ core holes like in HCl so that consideration of the sole Svensson propensity rule is sufficient in this case. For $M_{4,5}VV$ decay in HBr the situation is different and both propensity rules have to be considered. Note that previous results on the Auger decay of the oriented $4d^{-1}$ core holes in HI [7,58] also seem to follow this extended rule. It will be an interesting future target to check this with coincidence experiments, and to consider whether other molecules with $3d$ or $4d$ oriented core holes like Br$_2$ or I$_2$ obey the same propensity rules.

Finally, the present experimental setup allowed us to study for the case of well-defined kinetic energies of the Auger electron the influence of the PCI effect on the photoelectron spectrum. Complementary calculations of the PCI shift are performed. For Auger energies larger than 15 eV they agree well with the experimental results while for smaller values deviations are observed.

APPENDIX

As in the procedure of Johnsson *et al.* [24] the relativistic spin-orbit and molecular-field split core-hole states are obtained by adding to the nonrelativistic Hamiltonian an effective spin-orbit coupling operator:

$$\hat{H}_{\mathrm{SO}} = \xi_{\mathrm{Br}3d} \sum_{m,m'} |3d_{m'}\rangle \langle d_{m'}| \hat{\vec{l}} \cdot \hat{\vec{s}} |d_m\rangle \langle 3d_m|, \qquad (\mathrm{A1})$$

where $\xi_{\mathrm{Br}3d}$ is the Bromine $3d$ spin-orbit coupling parameter. The model (spin-orbit and molecular-field) Hamiltonian has the matrix representation

$$\begin{pmatrix} E(3d\delta^{-1})+\xi_{\mathrm{Br}3d} & 0 & 0 & 0 & 0 \\ 0 & E(3d\delta^{-1})-\xi_{\mathrm{Br}3d} & \xi_{\mathrm{Br}3d} & 0 & 0 \\ 0 & \xi_{\mathrm{Br}3d} & E(3d\pi^{-1})+\frac{\xi_{\mathrm{Br}3d}}{2} & 0 & 0 \\ 0 & 0 & 0 & E(3d\pi^{-1})-\frac{\xi_{\mathrm{Br}3d}}{2} & \sqrt{\frac{3}{2}}\xi_{\mathrm{Br}3d} \\ 0 & 0 & 0 & \sqrt{\frac{3}{2}}\xi_{\mathrm{Br}3d} & E(3d\sigma^{-1}) \end{pmatrix}, \qquad (\mathrm{A2})$$

in the basis of the core-hole configurations $3d\lambda^{-1}$ in the sequence $(3d\delta_+^{-1}, \overline{3d\delta_+}^{-1}, 3d\pi_+^{-1}, \overline{3d\pi_+}^{-1}, 3d\sigma^{-1})$ or $(\overline{3d\delta_-}^{-1}, 3d\delta_-^{-1}, \overline{3d\pi_-}^{-1}, 3d\pi_-^{-1}, \overline{3d\sigma}^{-1})$, which stand for the two degenerate Kramers doublets. Here, an overbar indicates a β-spin orbital while no overbar indicates an α-spin orbital. At π and δ orbitals the $+(-)$ subscript designates orbitals with positive (negative) expectation values for the rotation about the molecular axis. The experimental ionization potentials of the $3d_{j,m_j}^{-1}$ states [25] are obtained as eigenvalues of the Hamiltonian matrix in Eq. (A2) by using $\xi_{\mathrm{Br}3d} = -0.4125\,\mathrm{eV}$ [24] and the nonrelativistic core-hole energies given in Table I. The core-hole weights of the $3d\lambda^{-1}$

configurations of the $3d_{j,m_j}^{-1}$ state are the squares of the respective components of the corresponding eigenvectors. Please note that for the degenerate nonrelativistic core-hole states $[E(3d\delta^{-1}) = E(3d\pi^{-1}) = E(3d\sigma^{-1})]$, i.e., no molecular-field splitting, the state $3d_{5/2,3/2}^{-1}$ has a weight of 0.2 (0.8) for the $3d\delta^{-1}$ ($3d\pi^{-1}$) configuration while the state $3d_{5/2,1/2}^{-1}$ contains an amount of 0.4 (0.6) from the nonrelativistic $3d\pi^{-1}(3d\sigma^{-1})$ configuration. The weigths of the actual spin-orbit and molecular-field-split states in Table II deviate by 0.09 and 0.04 from these values for m_j values of 3/2 and 1/2, respectively, indicating the relatively strong molecular-field splitting. The latter is on the order of 0.33 eV and thus about one-third of the spin-orbit splitting ($\frac{5}{2}|\xi_{\text{Br}3d}| \approx 1$ eV) indicating an intermediate coupling case.

Using Eq. (A2) the Auger transition rates of the relativistic $3d_{j,m_j}^{-1}$ states can be related to those of nonrelativistic configurations. The latter are obtained in this paper according to the procedure presented in Refs. [9–11]. Thus, only the (spherically symmetric) atomic components centered at the core-hole atom are required and these are expanded into radial, R, and angular, Y, components as, e.g.,

$$\psi_v = R_v(r)Y_v(\vartheta, \varphi). \tag{A4}$$

The integration over the radial and angular parts of the two-electron integrals is separated by using the Laplace expansion providing

$$\langle c\varepsilon^{lm}|vv'\rangle = \sum_k R_k(c\varepsilon^l, vv')\frac{4\pi}{2k+1}$$
$$\times \sum_{q=-k}^{k} \langle Y_c \mid Y_k^{-q}Y_v\rangle\langle Y_l^m \mid Y_k^q Y_{v'}\rangle, \tag{A5}$$

where the angular integrals can be related to Clebsch-Gordan coefficients and the so-called Slater integrals are (see, e.g., [59])

$$R_k(c\varepsilon^l, vv') = \int_0^\infty \int_0^\infty R_c^*(r_1)R_{\varepsilon l}^*(r_2)\frac{r_<^k}{r_>^{k+1}}R_v(r_1)$$
$$\times R_{v'}(r_2)r_1^2 r_2^2 dr_1 dr_2. \tag{A6}$$

For the present case of d holes and s or p valence orbitals angular momentum quantum numbers of the continuum channel, l, are between zero and four. The Slater integrals for the $M_{4,5}NN$ Auger decays in Kr and Br obtained as

TABLE IV. Slater integrals normalized following the procedure given in Ref. [48] for the $M_{4,5}N_{1,2,3}N_{1,2,3}$ Auger decays of the Bromine and the Krypton atoms in atomic units.

$R_k(l_c l_\varepsilon, l_v l_{v'})$	Br	Kr
$R_1(20,11)$	0.003380	0.005126
$R_2(21,01)$	−0.040152	−0.035761
$R_1(21,10)$	−0.034111	−0.029106
$R_2(22,00)$	−0.091011	−0.083604
$R_1(22,11)$	−0.061545	−0.052556
$R_3(22,11)$	−0.052822	−0.048486
$R_2(23,01)$	−0.113179	−0.113431
$R_3(23,10)$	−0.081707	−0.084244
$R_3(24,11)$	0.040778	0.043253

described above are collected in Table IV where the orbitals are represented as usual by their angular momentum quantum numbers, l.

Using these data, a minimum model for the transition rates of the HBr molecule to the $4p\lambda^{-2}(\lambda = \sigma, \pi)$ final states is given as follows. We assume orthogonal orbitals for intermediate (core-hole) and final states as well as single-configuration representations of the final states. The Fermi "golden rule" transiton rate for the decay of a $3d\lambda^{-1}$ to a $^{2S+1}[vv']^{-2}$ final-state configuration, where $2S + 1$ is the spin multiplicity of the final state, is given by

$$I(3d\lambda^{-1} \rightarrow {}^1[vv']^{-2}) = \frac{2\pi}{\hbar}\frac{1}{2(1+\delta_{vv'})}\sum_{lm}(\langle 3d\gamma\,\varepsilon^{lm} \mid vv'\rangle$$
$$+ \langle 3d\gamma\,\varepsilon^{lm} \mid v'v\rangle)^2 \tag{A7}$$

and

$$I(3d\lambda^{-1} \rightarrow {}^3[vv']^{-2}) = \frac{2\pi}{\hbar}\frac{3}{2}\sum_{lm}(\langle 3d\gamma\,\varepsilon^{lm} \mid vv'\rangle$$
$$- \langle 3d\gamma\,\varepsilon^{lm} \mid v'v\rangle)^2 \tag{A8}$$

for singlet and triplet final states, respectively [48]. The Auger transition intensities to the $4p\lambda^{-2}$ final states are dominated by continuum channels with d character. Using just these contributions as well as atomic units, we obtain

$$I(3d\sigma^{-1} \rightarrow {}^3\Sigma^-[4p]^{-2}) = 2\pi\frac{3}{2}(\langle 3d\sigma\,\varepsilon^{20} \mid 4p\pi_+ 4p\pi_-\rangle - \langle 3d\sigma\,\varepsilon^{20} \mid 4p\pi_- 4p\pi_+\rangle)^2$$
$$= 3\pi(\langle 3d0\varepsilon d0|4p+14p-1\rangle - \langle 3d0\varepsilon d0|4p-14p+1\rangle)^2$$
$$= 3\pi(0.00796 - 0.00796)^2 = 0. \tag{A9}$$

This intensity has to be zero for symmetry reasons as it corresponds to a symmetry-forbidden Σ^+ to Σ^- transition. While the individual two electron matrix elements are not particularly small if compared with the corresponding ones for the other core-hole components, they sum up to zero. Furthermore, we obtain

$$I(3d\pi_+^{-1} \rightarrow {}^3\Sigma^-[4p]^{-2}) = 2\pi\frac{3}{2}(\langle 3d\pi_+\varepsilon^{2-1} \mid 4p\pi_+ 4p\pi_-\rangle - \langle 3d\pi_+\varepsilon^{2-1} \mid 4p\pi_- 4p\pi_+\rangle)^2$$
$$= 3\pi(\langle 3d+1\varepsilon d-1|4p+14p-1\rangle - \langle 3d+1\varepsilon d-1|4p-14p+1\rangle)^2$$
$$= 3\pi(-0.01421 + 0.00645)^2 = 0.568 \times 10^{-3} \tag{A10}$$

and

$$I(3d\delta_+{}^{-1} \to {}^3\Sigma^-[4p]^{-2}) = 2\pi \tfrac{3}{2}(\langle 3d\delta_+\varepsilon^{2-2}|4p\pi_+4p\pi_-\rangle - \langle 3d\delta_+\varepsilon^{2-2}|4p\pi_-4p\pi_+\rangle)^2$$
$$= 3\pi(\langle 3d+2\varepsilon d-2|4p+14p-1\rangle - \langle 3d+2\varepsilon d-2|4p-14p+1\rangle)^2$$
$$= 3\pi(0.02520 - 0.00968)^2 = 2.270 \times 10^{-3}. \tag{A11}$$

Differences to the values given in Table II are mostly due to the missing continuum g-channel contributions which amount to about 10% of the total intensity.

The transition to the degenerate ${}^1\Delta$ final state proceeds either to the $M_L = 2$ or -2 component of the final state. Starting from the $3d\sigma^{-1}$ core-hole state, both components can be reached via the ε^{22} and ε^{2-2} Auger channels leading to the total intensity

$$I(3d\sigma^{-1} \to {}^1\Delta[4p]^{-2}) = 2\pi \langle 3d\sigma\varepsilon^{22}|4p\pi_+4p\pi_+\rangle^2 + 2\pi \langle 3d\sigma\varepsilon^{2-2}|4p\pi_-4p\pi_-\rangle^2$$
$$= 2\pi(\langle 3d0\varepsilon d2|4p+14p+1\rangle^2 + \langle 3d0\varepsilon d-2|4p-14p-1\rangle^2)$$
$$= 2\pi(0.01160^2 + 0.01160^2) = 1.691 \times 10^{-3}. \tag{A12}$$

The decay of the other core-hole states proceeds only via one of these channels to one component of the ${}^1\Delta$ state:

$$I(3d\pi_+{}^{-1} \to {}^1\Delta[4p]^{-2}) = 2\pi(\langle 3d\pi_+\varepsilon^{21}|4p\pi_+4p\pi_+\rangle)^2$$
$$= 2\pi(\langle 3d+1\varepsilon d+1|4p+14p+1\rangle)^2$$
$$= 2\pi(-0.01421)^2 = 1.294 \times 10^{-3} \tag{A13}$$

and

$$I(3d\delta_+{}^{-1} \to {}^1\Delta[4p]^{-2}) = 2\pi(\langle 3d\delta_+\varepsilon^{20}|4p\pi_+4p\pi_+\rangle)^2$$
$$= 2\pi(\langle 3d+2\varepsilon d0|4p+14p+1\rangle)^2$$
$$= 2\pi(0.01160)^2 = 0.8454 \times 10^{-3}. \tag{A14}$$

In this case the individual integrals for the decay of the $3d\sigma^{-1}$ and $3d\delta^{-1}$ core-hole states are identical but they appear twice for the former due to the two available channels. Thus, the higher Auger transition rate of the $3d\sigma^{-1}$ hole configuration is due to the number of available channels.

In terms of the rotationally symmetric $4p\pi_\pm$ orbitals the ${}^1\Sigma^+$ $(4p\pi^{-2})$ final state is represented by the configuration ${}^1[4p\pi_+4p\pi_-]^{-2}$. Thus, the decay rates to this final state read

$$I(3d\sigma^{-1} \to {}^1\Sigma^+[4p]^{-2}) = 2\pi \tfrac{1}{2}(\langle 3d\sigma\varepsilon^{20}|4p\pi_+4p\pi_-\rangle + \langle 3d\sigma\varepsilon^{20}|4p\pi_-4p\pi_+\rangle)^2$$
$$= \pi(\langle 3d0\varepsilon d0|4p+14p-1\rangle + \langle 3d0\varepsilon d0|4p-14p+1\rangle)^2$$
$$= \pi(0.00796 + 0.00796)^2 = 0.7962 \times 10^{-3}, \tag{A15}$$

$$I(3d\pi_+{}^{-1} \to {}^1\Sigma^+[4p]^{-2}) = 2\pi \tfrac{1}{2}(\langle 3d\pi_+\varepsilon^{2-1}|4p\pi_+4p\pi_-\rangle + \langle 3d\pi_+\varepsilon^{2-1}|4p\pi_-4p\pi_+\rangle)^2$$
$$= \pi(\langle 3d+1\varepsilon d-1|4p+14p-1\rangle + \langle 3d+1\varepsilon d-1|4p-14p+1\rangle)^2$$
$$= \pi(-0.01421 - 0.00645)^2 = 1.3409 \times 10^{-3}, \tag{A16}$$

and

$$I(3d\delta_+{}^{-1} \to {}^1\Sigma^+[4p]^{-2}) = 2\pi \tfrac{1}{2}(\langle 3d\delta_+\varepsilon^{2-2}|4p\pi_+4p\pi_-\rangle + \langle 3d\delta_+\varepsilon^{2-2}|4p\pi_-4p\pi_+\rangle)^2$$
$$= \pi(\langle 3d+2\varepsilon d-2|4p+14p-1\rangle + \langle 3d+2\varepsilon d-2|4p-14pn+1\rangle)^2$$
$$= \pi(0.02520 + 0.00968)^2 = 3.822 \times 10^{-3}. \tag{A17}$$

These intensities are in quantitative agreement with Table II. As already mentioned above for the $4p\pi^{-2}$ ${}^3\Sigma^-$ final state the differences arise due to neglect of continuum channels other than d channels and due to admixture of other configurations to the

character of the final state. Nevertheless, all relative Auger intensity patterns are correctly reproduced. We note that the values of the Auger transition two electron integrals support the extended "Svensson" propensity rule for Auger decay proposed above.

[1] K. Siegbahn, C. Nordling, G. Johansson, J. Hedman, P. F. Heden, K. Hamrin, U. Gelius, T. Bergmark, L. O. Werme, R. Manne, and Y. Baer, *ESCA Applied to Free Molecules* (North-Holland, Amsterdam, 1969).

[2] U. Hergenhahn, J. Phys. B **37**, R89 (2004).

[3] B. Kempgens, H. Köppel, A. Kivimäki, M. Neeb, L. S. Cederbaum, and A. M. Bradshaw, Phys. Rev. Lett. **79**, 3617 (1997).

[4] O. Björneholm, J. Chem. Phys. **115**, 4139 (2001).

[5] J. N. Cutler, G. M. Bancroft, D. G. Sutherland, and K. H. Tan, Phys. Rev. Lett. **67**, 1531 (1991).

[6] S. Svensson, A. Naves de Brito, M. P. Keane, N. Correia, and L. Karlsson, Phys. Rev. A **43**, 6441 (1991).

[7] S. Svensson, A. Ausmees, S. J. Osborne, G. Bray, F. Gel'mukhanov, H. Ågren, A. Naves de Brito, O.-P. Sairanen, A. Kivimäki, E. Nõmmiste, H. Aksela, and S. Aksela, Phys. Rev. Lett. **72**, 3021 (1994).

[8] F. Gel'mukhanov, H. Ågren, S. Svensson, H. Aksela, and S. Aksela, Phys. Rev. A **53**, 1379 (1996).

[9] R. F. Fink, M. Kivilompolo, H. Aksela, and S. Aksela, Phys. Rev. A **58**, 1988 (1998).

[10] R. F. Fink, A. Eschner, M. Magnuson, O. Björneholm, I. Hjelte, C. Miron, M. Bässler, S. Svensson, M. N. Piancastelli, and S. L. Sorensen, J. Phys. B **39**, L269 (2006).

[11] A. Machado Bueno, A. Naves de Brito, R. F. Fink, M. Bässler, O. Björneholm, F. Burmeister, R. Feifel, C. Miron, S. L. Sorensen, H. Wang, and S. Svensson, Phys. Rev. A **67**, 022714 (2003).

[12] M. Poygin, R. Püttner, M. Martins, V. Pennanen, M. Jurvansuu, Y. H. Jiang, H. Aksela, S. Aksela, and G. Kaindl, Phys. Rev. A **74**, 012711 (2006).

[13] J. H. D. Eland, R. F. Fink, P. Linusson, L. Hedin, S. Plogmaker, and R. Feifel, Phys. Chem. Chem. Phys. **13**, 18428 (2011).

[14] O. Travnikova, R. F. Fink, A. Kivimäki, D. Céolin, Z. Bao, and M. N. Piancastelli, Chem. Phys. Lett. **474**, 67 (2009).

[15] V. Sekushin, R. Püttner, R. F. Fink, M. Martins, Y. H. Jiang, H. Aksela, S. Aksela, and G. Kaindl, J. Chem. Phys. **137**, 044310 (2012).

[16] Y. Hikosaka, M. Sawa, K. Soejima, and E. Shigemasa, J. Electron Spectrosc. Relat. Phenom. **192**, 69 (2014).

[17] R. Püttner, V. Pennanen, T. Matila, A. Kivimäki, M. Jurvansuu, H. Aksela, and S. Aksela, Phys. Rev. A **65**, 042505 (2002).

[18] R. Püttner, Y. F. Hu, G. M. Bancroft, H. Aksela, E. Nõmmiste, J. Karvonen, A. Kivimäki, and S. Aksela, Phys. Rev. A **59**, 4438 (1999).

[19] B. Wannberg, S. Svensson, M. P. Keane, L. Karlsson, and P. Baltzer, Chem. Phys. **133**, 281 (1989).

[20] J. H. Eland, Chem. Phys. **294**, 171 (2003).

[21] M. Alagia, B. G. Brunetti, P. Candori, S. Falcinelli, M. M. Teixidor, F. Pirani, R. Richter, S. Stranges, and F. Vecchiocattivi, J. Chem. Phys. **120**, 6980 (2004).

[22] T. Matila, K. Ellingsen, T. Saue, H. Aksela, and O. Gropen, Phys. Rev. A **61**, 032712 (2000).

[23] Z. F. Liu, G. M. Bancroft, K. H. Tan, and M. Schachter, J. Electron Spectrosc. Relat. Phenom. **67**, 299 (1994).

[24] J. Johnson, J. N. Cutler, G. M. Bancroft, Y. F. Hu, and K. H. Tan, J. Phys. B **30**, 4899 (1997).

[25] Y. F. Hu, Z. F. Liu, R. Püttner, G. M. Bancroft, and S. Aksela, J. Phys. B **32**, 4091 (1999).

[26] T. Matila, R. Püttner, A. Kivimäki, H. Aksela, and S. Aksela, J. Phys. B **35**, 4607 (2002).

[27] K. J. S. Sawhney, F. Senf, M. Scheer, F. Schäfers, J. Bahrdt, A. Gaupp, and W. Gudat, Nucl. Instrum. Methods Phys. Res. Sect. Accel. Spectrometers Detect. Assoc. Equip. **390**, 395 (1997).

[28] K. Ito, F. Penent, Y. Hikosaka, E. Shigemasa, I. H. Suzuki, J. H. D. Eland, and P. Lablanquie, Rev. Sci. Instrum. **80**, 123101 (2009).

[29] F. Penent, P. Lablanquie, J. Palaudoux, L. Andric, G. Gamblin, Y. Hikosaka, K. Ito, and S. Carniato, Phys. Rev. Lett. **106**, 103002 (2011).

[30] J. Palaudoux, S. Sheinerman, J. Soronen, S.-M. Huttula, M. Huttula, K. Jänkälä, L. Andric, K. Ito, P. Lablanquie, F. Penent, J.-M. Bizau, S. Guilbaud, and D. Cubaynes, Phys. Rev. A **92**, 012510 (2015).

[31] M. Y. Kuchiev and S. A. Sheinerman, Sov. Phys. JETP **63**, 986 (1986).

[32] P. van der Straten, R. Morgenstern, and A. Niehaus, Z. Fr Phys. At. Mol. Clust. **8**, 35 (1988).

[33] E. Kukk, G. Snell, J. D. Bozek, W.-T. Cheng, and N. Berrah, Phys. Rev. A **63**, 062702 (2001).

[34] E. Kukk, K. Ueda, U. Hergenhahn, X.-J. Liu, G. Prümper, H. Yoshida, Y. Tamenori, C. Makochekanwa, T. Tanaka, M. Kitajima, and H. Tanaka, Phys. Rev. Lett. **95**, 133001 (2005).

[35] G. B. Armen, J. Tulkki, T. Aberg, and B. Crasemann, Phys. Rev. A **36**, 5606 (1987).

[36] R. Fink, J. Chem. Phys. **106**, 4038 (1997).

[37] S. L. Sorensen, R. Fink, R. Feifel, M. N. Piancastelli, M. Bässler, C. Miron, H. Wang, I. Hjelte, O. Bjorneholm, and S. Svensson, Phys. Rev. A **64**, 012719 (2001).

[38] K. Wiesner, R. Fink, S. Sorensen, M. Andersson, R. Feifel, I. Hjelte, C. Miron, A. Naves de Brito, L. Rosenqvist, H. Wang, S. Svensson, and O. Björneholm, Chem. Phys. Lett. **375**, 76 (2003).

[39] U. Hergenhahn, A. Rüdel, K. Maier, A. M. Bradshaw, R. F. Fink, and A. T. Wen, Chem. Phys. **289**, 57 (2003).

[40] K. P. Huber and G. Herzberg, *Molecular Spectra and Molecular Structure* (Springer, New York, 1979).

[41] T. H. Dunning, J. Chem. Phys. **90**, 1007 (1989).

[42] A. K. Wilson, D. E. Woon, K. A. Peterson, and T. H. Dunning, J. Chem. Phys. **110**, 7667 (1999).

[43] H. Siegbahn, L. Asplund, and P. Kelfve, Chem. Phys. Lett. **35**, 330 (1975).

[44] H. Ågren, S. Svensson, and U. I. Wahlgren, Chem. Phys. Lett. **35**, 336 (1975).

[45] R. Fink, J. Electron Spectrosc. Relat. Phenom. **76**, 295 (1995).

[46] S. Fritzsche, J. Electron Spectrosc. Relat. Phenom. **114–116**, 1155 (2001).

[47] S. Fritzsche, Phys. Scr. **T100**, 37 (2002).

[48] E. Z. Chelkowska and F. P. Larkins, At. Data Nucl. Data Tables **49**, 121 (1991).

[49] M. H. Chen, F. P. Larkins, and B. Crasemann, At. Data Nucl. Data Tables **45**, 1 (1990).

[50] R. F. Fink, M. N. Piancastelli, A. N. Grum-Grzhimailo, and K. Ueda, J. Chem. Phys. **130**, 014306 (2009).

[51] M. K. Odling-Smee, E. Sokell, A. A. Wills, and P. Hammond, J. Phys. B **32**, 2529 (1999).

[52] S. Sheinerman, P. Lablanquie, F. Penent, J. Palaudoux, J. H. D. Eland, T. Aoto, Y. Hikosaka, and K. Ito, J. Phys. B At. Mol. Opt. Phys. **39**, 1017 (2006).

[53] J. H. D. Eland, Chem. Phys. Lett. **409**, 245 (2005).

[54] M. Y. Kuchiev and S. A. Sheinerman, J. Phys. B **21**, 2027 (1988).

[55] D. Rolles, G. Prümper, H. Fukuzawa, X.-J. Liu, Z. D. Pešić, R. F. Fink, A. N. Grum-Grzhimailo, I. Dumitriu, N. Berrah, and K. Ueda, Phys. Rev. Lett. **101**, 263002 (2008).

[56] R. Püttner, Y. F. Hu, G. M. Bancroft, A. Kivimäki, M. Jurvansuu, H. Aksela, and S. Aksela, Phys. Rev. A **68**, 032705 (2003).

[57] V. Schmidt, *Electron Spectroscopy of Atoms Using Synchrotron Radiation* (Cambridge University, Cambridge, England, 1997).

[58] L. Karlsson, S. Svensson, P. Baltzer, M. Carlsson-Gothe, M. P. Keane, A. N. de Brito, N. Correia, and B. Wannberg, J. Phys. B **22**, 3001 (1989).

[59] C. Froese-Fischer, T. Brage, and P. Jönsson, *Computational Atomic Structure A MCHF Approach* (Institute of Physics Publishing, London, 1997).